Energy and Buildings 138 (2017) 140–153

Contents lists available at ScienceDirect

Energy and Buildings

journal homepage: www.elsevier.com/locate/enbuild

An experimental and numerical study on fire behaviors of charring materials frequently used in buildings

Long Shi [a,*], Michael Yit Lin Chew [b], Xuanya Liu [c], Xudong Cheng [d], Bo Wang [e], Guomin Zhang [a]

[a] Civil and Infrastructure Engineering Discipline, School of Engineering, RMIT University, Melbourne, VIC 3001, Australia
[b] Department of Building, National University of Singapore, 117566, Singapore
[c] Tianjin Fire Research Institute of MPS of China, No. 110, South Weijin Road, Nankai District, Tianjin, 300382, PR China
[d] State Key Laboratory of Fire Science, University of Science and Technology of China, Hefei, Anhui, 230026, PR China
[e] College of Mathematics and Computer Science, Hunan Normal University, Changsha, Hunan, 410081, PR China

ARTICLE INFO

Article history:
Received 4 August 2016
Received in revised form 25 October 2016
Accepted 10 December 2016
Available online 12 December 2016

Keywords:
Building material
Charring material
Timber
Polymer
Fire behavior
Numerical modeling

ABSTRACT

The single biggest market barriers of building materials is their fire risks, suffering from easily burning and generating a large amount of smoke and toxic gases. Fire behaviors of typical charring materials, including timber (Cherry) and polymer (acrylonitrile butadiene styrene, ABS), were investigated both experimentally and numerically. The proposed numerical model has considered both solid (the area inside sample slab) and gas (the area above sample surface) phases, addressing some previously usually-ignored fire processes, such as water evaporation, gases and liquids transportation inside solids, and volume change. Numerical results of timber and polymer were validated by cone calorimeter experiments. From both experimental and numerical results, three different stages of mass loss rate histories of charring materials were observed under external heat flux. In the gas phase, three high temperature areas were observed: two are near the walls of the two heaters due to the convection heat transfer; and one represents diffusion flame above sample surface, in which temperature increases with the intensity of external heat flux. This study provides not only an attempt to combine both solid and gas phases modeling for building materials, but also a platform for fire behavior modeling. Future research will focus on the validation of gas phase modeling and implementation of flame radiation.

1. Introduction

Charring materials such as timber and polymer have attracted great attention because of the increasing demands as construction materials in buildings. Timber as a traditional material has been widely used for numerous applications in construction sector, such as framing, flooring, roofing and lining [1]. In Australia, it is the most commonly used material for structural frames and one of the two common types of floor design besides concrete [2]. Acrylonitrile butadiene styrene (ABS) is also an important engineering copolymer because of its superior mechanical properties, chemical resistance, ease of processing, and recyclability, with various applications in buildings and relevant constructions, such as personal care products, computer equipment and interior components [3]. The single biggest market barriers of these building materials is their fire risks, suffering from easily burning and generating a large amount of smoke and toxic gases [4,5].

Understanding the thermal and chemical impacts of burning energetic materials in both normal use and accidental scenarios is becoming increasingly relevant [6]. Fire behaviors of these charring materials are generally complicated and involves a mix of chemical, physical and mechanical processes (such as volume change [7,8]). A recent review has addressed four main fire processes involved in fire development of charring materials, including thermal, physical, chemical and failure processes [9]. It is obtained that some fire processes (i.e. water evaporation, gas and liquid transportation inside solid materials, and volume change) are usually ignored during previous studies, and less studies have been focused on the fire behavior modeling of some complicated charring polymers. Fig. 1 shows the main fire processes of charring materials under external heat flux.

Numerical modeling has been frequently used to evaluate building designs, but fire source modeling is still a challenge in term of modeling accuracy and flexibility. For example, time square increasing fire (sometimes even constant fire source) is usually

* Corresponding author.
E-mail addresses: shilong@mail.ustc.edu.cn, long.shi@rmit.edu.au (L. Shi).

http://dx.doi.org/10.1016/j.enbuild.2016.12.035
0378-7788/

Nomenclature

A	Pre-exponential frequency factor (s^{-1})
ΔH	Heat of reaction (J/kg)
C_p	Specific heat capacity ($J\,kg\,K^{-1}$)
Θ	Production or reaction rate ($kg\,m^3\,s^{-1}$)
D	Diffusivity coefficient ($m^2\,s^{-1}$)
ε	Emissivity of materials (–)
E	Activation energy ($J\,mol^{-1}$)
λ	Thermal conductivity ($W\,m\,K^{-1}$)
h	Heat transfer coefficient ($W\,m\,K^{-1}$)
μ	Dynamic viscosity (Pa s)
H	Specific enthalpy of materials (J)
υ	Viscosity, stoichiometric coefficient
k	Reaction rate constant (s^{-1})
ρ	Density ($kg\,m^3$)
L	Thickness (m)
σ	Stefan-Boltzmann constant ($W\,m^2\,K^{-4}$)
$\dot{m}''$	Mass flux ($kg\,m^2\,s^{-1}$)
ϕ	Porosity (–)
M	Molecular weight ($kg\,mol^{-1}$)
n	Order of reaction (–)

Subscript and superscript

N	Number of species
0	Initial or ambient condition
P	Pressure (Pa)
B	Bottom boundary
$\dot{q}''$	Heat flux ($W\,m^2$)
cond	Conductivity
Q	Heat of reaction ($W\,m^3$)
conv	Convection process
R	Universal gas constant ($J\,mol^{-1}\,K^{-1}$)
ext	External
t	Time (s)
ex	Term at the exit
T	Absolute temperature (K)
fuel	General designation of gases volatiles
u, v	Velocity ($m\,s^{-1}$)
g	Gas phase, gas species
x, y	Cartesian coordinate (m)
l	Liquid water
X	Moisture content (–)
loss	Loss
Y	Mass fraction (–)
pyr	Pyrolysis process
rad	Radiation process

Greek letters

reac	Reaction process
γ	Permeability (m^2)
s	Solid phase, solid species
κ	Absorption coefficient (m^{-1})
sur	Surface
Δ	Change in variable value (–)
theor	Theoretical value

assumed for the related building designs and evaluation [10]. This assumption shows a good prediction of overall fire behavior for single compartment, but the difference is quite obvious for single item, such as furniture. Therefore, many studies have been focused on the improvement of fire source modelling. The major achievements of previously developed numerical models are: (*i*) one-dimensional modeling of the single solid phase, including homogeneous and

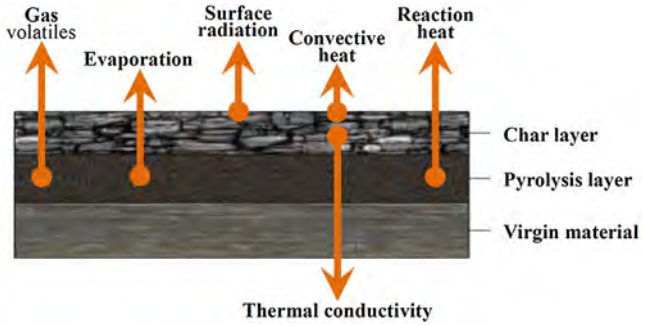

Fig. 1. Fire processes of charring materials under external heat flux.

heterogeneous pyrolysis reactions of virgin timber [11,12], non-charring polymers [13,14], charring polymers [15,16], as well as few intumescent polymers [17]; (*ii*) ability to model more than one type of solids (Gpyro [18] and ThermaKin [19]); and (*iii*) prediction of transport rates of gas volatiles away from the solid phase.

However, it is still a challenge to develop a numerical model that can simulate both solid and gas phases. Almost all previous studies in the area of pyrolysis modeling have focuses on single solid phase, leaving the gap on combining both phases. Another challenge is that there is no common agreement on some of the fire processes. For example, many models have considered volume change under external radiation, but no common agreement exists about its description or influences. Descriptions of volume change in previous numerical models were linked with pore volume [20], mass conversion [21,22], volume change factor [23–26], experimental data [27–30], production rate of gas volatiles [31], shrinkage factor [32], or shrinkage velocity profile [26].

Several aspects must be considered to improve the modelling accuracy, such as internal gas pressure and other important physical processes. This is even mandatory when the solid and gas phases modelling are combined. Accurate description of some physical processes, such as evaporation, is also critical to the numerical modelling [33]. For example, although gas species can hardly pass through polymer slab under normal condition, volatiles can exhaust from solid slab under irradiance [34]. The reason is the development of melted polymer and/or char layers. Internal gas pressure is important to descript the liquid and gas transportation inside the solid phase, which is also affected by the some of the parameters, such as permeability and porosity.

Some fire processes in previous studies have either not been previously considered at all, or have not been considered simultaneously. Very few numerical models have considered gas phase (diffusion flame modeling). A combination of integrated solid phase modeling and gas phase is critically important. Numerical methods for gas phase modeling are quite mature [35], but the relevant studies on solid phase modeling are relatively less investigated. This is partly because of the difficult-to-described fire processes encountered in numerical modeling. For example, there is still facing difficulty in describing some processes under fire conditions, such as gas and liquid transportation inside the solid slabs [36,37]. In addition, for previous models, one-dimensional modelling was usually utilized as it is enough to describe the processes in the sold phase when the edges and bottom are covered for insulation [9]. Another reason is because the three-dimensional model can experience very long CPU calculation time [38], which is not the level for practical applications under current computing resources.

Therefore, to improve fire source modeling, fire behaviors of charring materials frequently used in buildings were investigated in both solid and gas phases both experimentally and numerically, considering some important processes such as melting of solid, water evaporation, volume change and internal gas and liq-

uid transportation. In addition, the present study offers extended experimental validation of the model against full combustion history of burning samples. It provides not only an attempt to combine both solid and gas phases modeling of building materials, but also a platform for building fire modeling.

2. Experimental set-up

The left part in Fig. 2 shows experimental set-up of cone calorimeter. During experiments, cone calorimeter was positioned under a bigger hood and the volume extraction rate was keeping at 24 L/s. The volume extraction provides a forced convection driven flow under the cone calorimeter. The cone heater, located above the sample surface, provides constant heat flux on the sample surface. External heat fluxes were chosen to represent low, middle and high radiation, represented by heat fluxes of 25, 50 and 75 kW/m^2, respectively.

The edge and bottom of all of tested samples were covered by insulation materials, following the ISO 5660-1 [39]. After that, sample was put in horizontal orientation on specimen holder. Spark plug was not used during whole experimental time, and autoignition of the samples was considered to occur when visible flame was first observed. All the experiments were stopped when the flame was extinguished. Each experiment was repeated at least two times, with more runs taken if the repeatability was not good. More details of the experiments can be found in References [40,41].

3. Mathematical model

3.1. Major assumptions

The major features and equations are briefly introduced here, and further details can be seen in our previous studies [42,43]. The major features of the proposed model include: (*i*) it models both the gas phase (the area above the sample surface) and solid phase (the area inside the sample slab); (*ii*) consideration of three types of transformations, including physical/mechanical processes, as well as heterogeneous and homogeneous chemical reactions, makes it capable of describing water evaporation, solid melting, and pyrolysis and oxidation reactions; and (*iii*) consideration of permeability and porosity makes it capable of simulating liquid and gas transportation processes inside the solid phase.

Schematic of a computational domain is shown in the right part of Fig. 2. Several assumptions were adopted for this model: (*i*) solid phase was considered as one-dimensional, and the gas phase as two-dimensional, which are due to the predominant (normal) direction of heat transfer in the solid phase and simplicity of equivalent cross-sectional areas in the gas phase, respectively; (*ii*) homogeneous reactions in the solid phase were ignored, which were considered in the gas phase only; (*iii*) all gas species have the same thermal properties. Gas species in the solid phase were assumed to be ideal gases, and gas species in the gas phase were treated as incompressible ideal gas; (*iv*) the influences of the changed sample thickness on the gas phase combustion processes was ignored, which is because the changed sample thickness has limited influence on chemical reactions happened in the gas phase; (*v*) failure processes such as cracking were ignored due to the complexity; and (*vi*) thermal feedback from flame to charring material was assumed to be negligible compared to external radiation.

3.2. Governing equations

3.2.1. The solid phase

The main objective of the solid phase modeling is to describe the related thermal, chemical, and physical processes happened after the sample slabs were positioned under external heat flux. The related thermal processes include the radiation absorption on the sample surface, convective heat between the surface and surrounding airflows, the heat transfer to the bottom side, and reaction heat released from pyrolysis reactions. The chemical reactions are mainly about the pyrolysis reactions of virgin material and its products. Physical processes include the volume change, gas and liquid transportation inside the solid slabs. The details can be seen in Fig. 1. The following contents will focused on describing these three main processes.

Conservation equations in the solid phase describe the main processes in the solid phase, which are given as

$$\sum_{i=1}^{N_s+N_l+N_g} \frac{\partial \rho_i \phi C_{p,i} T_s}{\partial t} + \sum_{j=1}^{N_l+N_g} \frac{\partial \rho_j \phi C_{p,j} T_s u_j}{\partial x} = \frac{\partial}{\partial x}\left(\lambda \frac{\partial T_s}{\partial x}\right) + Q_{pyr} + \frac{\partial \dot{q}''_{rad}}{\partial x} \tag{1}$$

$$\frac{\partial \rho_i}{\partial t} = \Theta_i \tag{2}$$

$$\frac{\partial \rho_g \phi}{\partial t} + \frac{\partial \rho_g \phi u}{\partial x} = -\left(\Theta_i + \Theta_l\right) \tag{3}$$

$$\frac{\partial \rho_l}{\partial t} + \frac{\partial \rho_l u}{\partial x} = \Theta_l \tag{4}$$

Here Eq. (1) describes the energy conservation equation, while the two terms on the left hand side are the transient energy and convective heat terms, respectively, and the three terms on the right hand side describe heat conduction, pyrolysis reaction heat and external radiation term, respectively; Eq. (2) is the consumption of solid species; and Eqs. (3) and (4) represent the mass conservations for gas and liquid, respectively. For Eqs. (3) and (4), the left hand side describes the transient and convective terms, while the right hand side includes the production rate of solid or liquid species.

The heat released from pyrolysis reactions was introduced in Eq. (1), but pyrolysis kinetics for materials in practical use is fairly complicated, and composition of their volatiles is difficult to quantify. Therefore, decomposition is being esimated in this study by chemical reactions of the form

$$\nu^j_{1s}[S]^j_{1s} + \nu^j_{1g}[G]^j_{1g} \xrightarrow{k_j} \nu^j_{2s}[S]^j_{2s} + \nu^j_{2g}[G]^j_{2g} + \Delta H_j \tag{5}$$

where ν is the coefficient of the pyrolysis reactions, which is written on a mass basis, and with kinetic parameters evaluated from available data [44–47]. Here [S] stands for solid species and [G] stands for gas species.

Eqs. (1)–(4) are supplemented by the constitutive relations (Darcy's law) applying to both gas and liquid flows through the porous matrix of the material. The principle of the Darcy's law is to describe the flow in porous media under pressure gradient, which is expressed by

$$u_g = -\frac{\gamma_g}{\mu_g \phi}\frac{\partial P}{\partial x},\ u_l = -\frac{\gamma_l}{\mu_l}\frac{\partial P}{\partial x} \tag{6}$$

Here γ is the permeability of the solid phase; and the pressure inside the solid phase, P, can be calculated from the ideal gas law

$$P = \rho_g R T / M_g \tag{7}$$

where M_g is the molecular weight of the gas mixture

$$M_g = \left(\sum_{i=1}^{N_g} \frac{Y_i}{M_i}\right)^{-1} \tag{8}$$

Porosity of the solid can be assumed regarding its density [48]:

$$\phi = 1 - (\rho_{theor})^{-1} \sum_{i=1}^{N_s} \rho_i \tag{9}$$

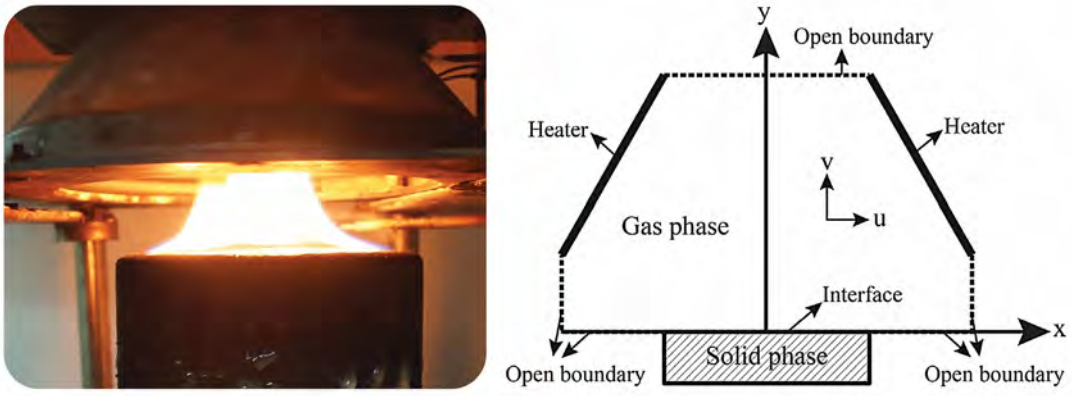

Fig. 2. Experimental set-up (left) and computational domain of FiresCone (right).

using ρ_{theor} as a theoretical (usually assumed to be 1500 kg/m^3 [48]).

The terms in Eqs. (2)–(4)are utilized to describe the production rate of products from those pyrolysis reactions, which can be given by

$$\Theta_i = \sum_j \nu_{1s}^j k_j \rho_j^{n_j}; k_j = A_j \exp\left(-E_j/RT\right); \Theta_l = A_l \cdot \exp\left(-E_l/RT\right) \rho_l \tag{10}$$

The latter Arrhenius kinetics treatment in Eq. (10) is justified in the case of water embedded as moisture into the porous matrix of the material, effectively without free surface [49].

It was assumed that the volume of each grid is related to the volumes of the all the solid and liquid species, including virgin material and its pyrolysis products. The grid size can be then estimated by summing up the volumes of all the solid and liquid species

$$\Delta x = \Delta x_0 \sum_{i=1}^{N_S+N_l} \frac{\rho_i}{\rho_{i,0}} \tag{11}$$

Heat generated or absorbed during pyrolysis reactions, introduced in Eq. (1), is given by

$$Q_{pyr} = \sum_j \Delta H_j \Theta_j \tag{12}$$

Absorption of radiation, the last term in Eq. (1), is described following the Beer-Lambert Law

$$\dot{q}''_{rad} = \dot{q}''_{ext} \exp(-\kappa x) \tag{13}$$

In Section 4, the predicted mass loss rate (*MLR*) of this model will be validated by cone calorimeter experiments. During the numerical modeling, *MLR* of solid slab is calculated based on the transient mass loss of all the solid and liquid species. Gas species were ignored during the calculation as they can exhaust to the gas phase fast. The mass loss rate of the solid slab can be given by

$$MLR = -\frac{\partial}{\partial t}\left(\sum_{i=1}^{N_S+N_l} \rho_i \Delta x_i\right) \tag{14}$$

Thermal properties, such as diffusion coefficient, permeability, radiation absorption coefficient, emissivity and thermal conductivity, are much dependent on the volume of the materials. So they were estimated based on volume fraction

$$U = \left(\sum_{i=1}^{N_s+N_l} \frac{\rho_i}{\rho_{i,0}}\right)^{-1} \sum_{i=1}^{N_s+N_l} U_i \frac{\rho_i}{\rho_{i,0}}, U = \gamma, D, \varepsilon, \kappa, \lambda \tag{15}$$

Thermal properties, such as specific heat capacity, were calculated based on mass fraction as those properties are much affected by the mass of the material

$$U = \left(\sum_{i=1}^{N_s+N_l} \rho_i\right)^{-1} \sum_{i=1}^{N_s+N_l} \rho_i U_i, U = C_P \tag{16}$$

3.2.2. The gas phase

The objective of gas phase modeling is to simulate the combustion processes of those gas volatiles exhausted from the solid phase. These gas volatiles go through combustion processes when they meet the oxygen under high temperature. Two-dimensional Navier-Stokes equations, supplemented with the continuity, energy and species conservation equations, are then utilized to simulate the combustion behavior in the gas phase

$$\frac{\partial \rho C_p T}{\partial t} + \frac{\partial \rho C_p u T}{\partial x} + \frac{\partial \rho C_p v T}{\partial y} = \frac{\partial}{\partial x}\left(\lambda \frac{\partial T}{\partial x}\right) + \frac{\partial}{\partial y}\left(\lambda \frac{\partial T}{\partial y}\right) + Q_{reac} \tag{17}$$

$$\frac{\partial u}{\partial x} + \frac{\partial v}{\partial y} = 0 \tag{18}$$

$$\frac{\partial \rho u}{\partial t} + \frac{\partial \rho u u}{\partial x} + \frac{\partial \rho v u}{\partial y} = \frac{\partial}{\partial x}\left(\mu \frac{\partial u}{\partial x}\right) + \frac{\partial}{\partial y}\left(\mu \frac{\partial u}{\partial y}\right) - \frac{\partial P}{\partial x} \tag{19}$$

$$\frac{\partial \rho v}{\partial t} + \frac{\partial \rho u v}{\partial x} + \frac{\partial \rho v v}{\partial y} = \frac{\partial}{\partial x}\left(\mu \frac{\partial v}{\partial x}\right) + \frac{\partial}{\partial y}\left(\mu \frac{\partial v}{\partial y}\right) - \frac{\partial P}{\partial y} \tag{20}$$

$$\frac{\partial \rho Y_i}{\partial t} + \frac{\partial \rho u Y_i}{\partial x} + \frac{\partial \rho v Y_i}{\partial y} = \frac{\partial}{\partial x}\left(\rho D \frac{\partial Y_i}{\partial x}\right) + \frac{\partial}{\partial y}\left(\rho D \frac{\partial Y_i}{\partial y}\right) + \Theta_{reac} \tag{21}$$

where Eq. (17) is the energy conservation equation for the gas phase modeling, considering heat conduction and combustion reaction heat, listed on the right hand side of this equation; Eq. (18) is the continuity equation; Eqs. (19) and (20) are the momentum equations in the X and Y direction, as shown in Fig. 2; and Eq. (21) is the gas species equation.

In the absence of detailed information on the chemical composition of pyrolysis products (which is quite complex and difficult to quantify precisely), the chemical reaction in the diffusion flame for the gas phase modeling, introduced in Eq. (17), is written in a general form on mass basis

$$[F] + \nu_{O_2}[O_2] \xrightarrow{kf} \nu_{CO}[CO] + \nu_{CO_2}[CO_2] + \nu_{H_2O} + H_2O + \Delta H_f \tag{22}$$

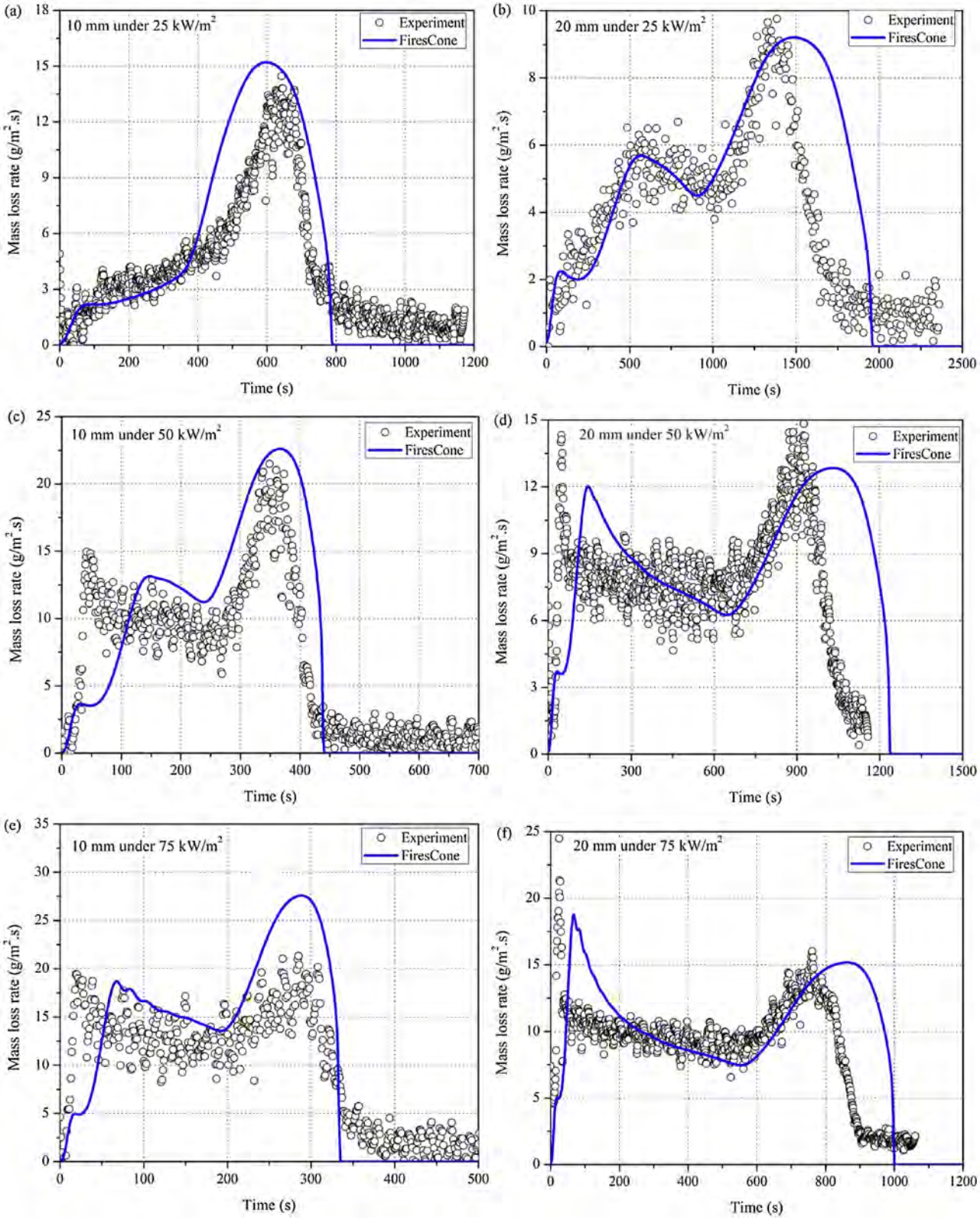

Fig. 3. Comparisons between modeling and experiments for 10 and 20 mm thick Cherry samples under 25–75 kW/m² heat flux.

with the reaction rate constant and the rate of heat release given by

$$k_f = A_f \cdot \exp\left(-E_f/RT\right);\ Q_{reac} = k_f \rho Y_F \cdot Y_{O_2} \cdot \Delta H_f \qquad (23)$$

Relevant stoichiometric and kinetic parameters are listed in Tables 1 and 2.

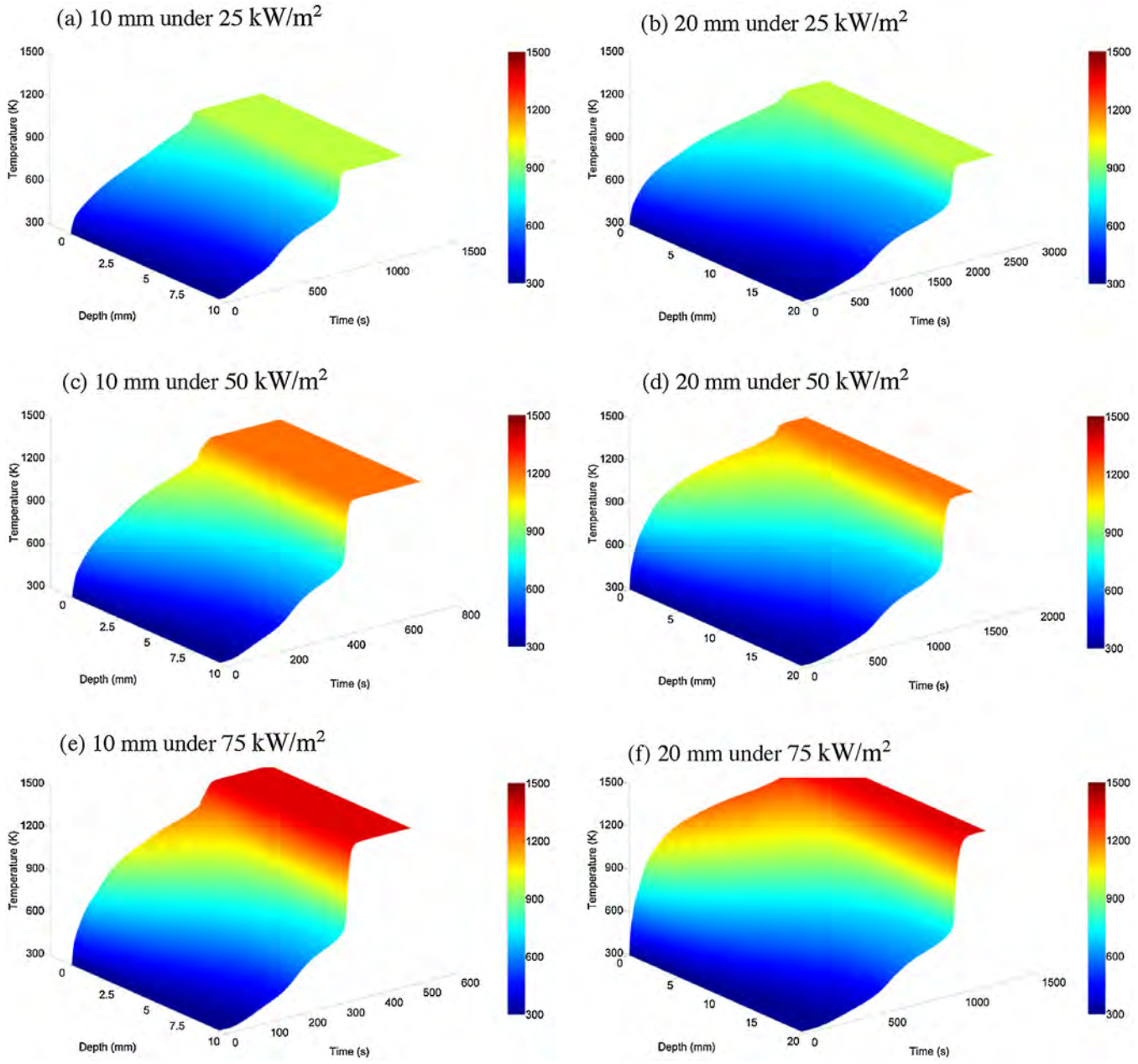

Fig. 4. Temperatures inside 10 and 20 mm thick Cherry samples under 25–75 kW/m^2 heat flux.

Table 1
Thermal properties of Cherry for modeling input.

Property	Unit	Cherry	Char/Ash	Water	Gas
Pyrolysis reaction rate	1/s	2.49×10^6 exp(−106500/RT) [9]	1.31×10^8 exp(−134000/RT) [12]	4.29×10^3 exp(−43800/RT) [53]	–
Density	kg/m^3	558 [Measured]	350 (char) [54]; 35 (Ash)	1000	1.205
Moisture content	kg/kg	0.113 [Measured]	–	–	–
Yield	kg/kg	0.26 (char) [9]	0.2 (Ash yield)	–	–
Heat of reaction	J/kg	4.18×10^5 [55]	9.8×10^5	2.45×10^6 [56]	–
Heat transfer coefficient	W/m^2 K	10 [57]	10	–	–
Gas permeability	m^2	5.80×10^{-17} [58]	5.80×10^{-17}	–	–
Water permeability	m^2	3.79×10^{-20} [59]	3.79×10^{-20}	–	–
Diffusion coefficient of water	m^2/s	5.11×10^{-9} [58]	5.11×10^{-8}	5.11×10^{-8}	–
Diffusion coefficient of gas	m^2/s	1.85×10^{-10} [60]	1.85×10^{-9}	1.85×10^{-9}	–
Specific heat capacity	J/kg K	3200 [61]	1350 [62]	4183 [63]	1000 [64]
Surface emissivity	–	0.76 [9]	0.80 [65]	0.97 [66]	–
Thermal conductivity	W/m K	0.35 [67]	0.18	0.61 [68]	0.03 [67]
Dynamic viscosity	Pa s	–	–	8.9×10^{-4} [69]	2.0×10^{-5} [70]

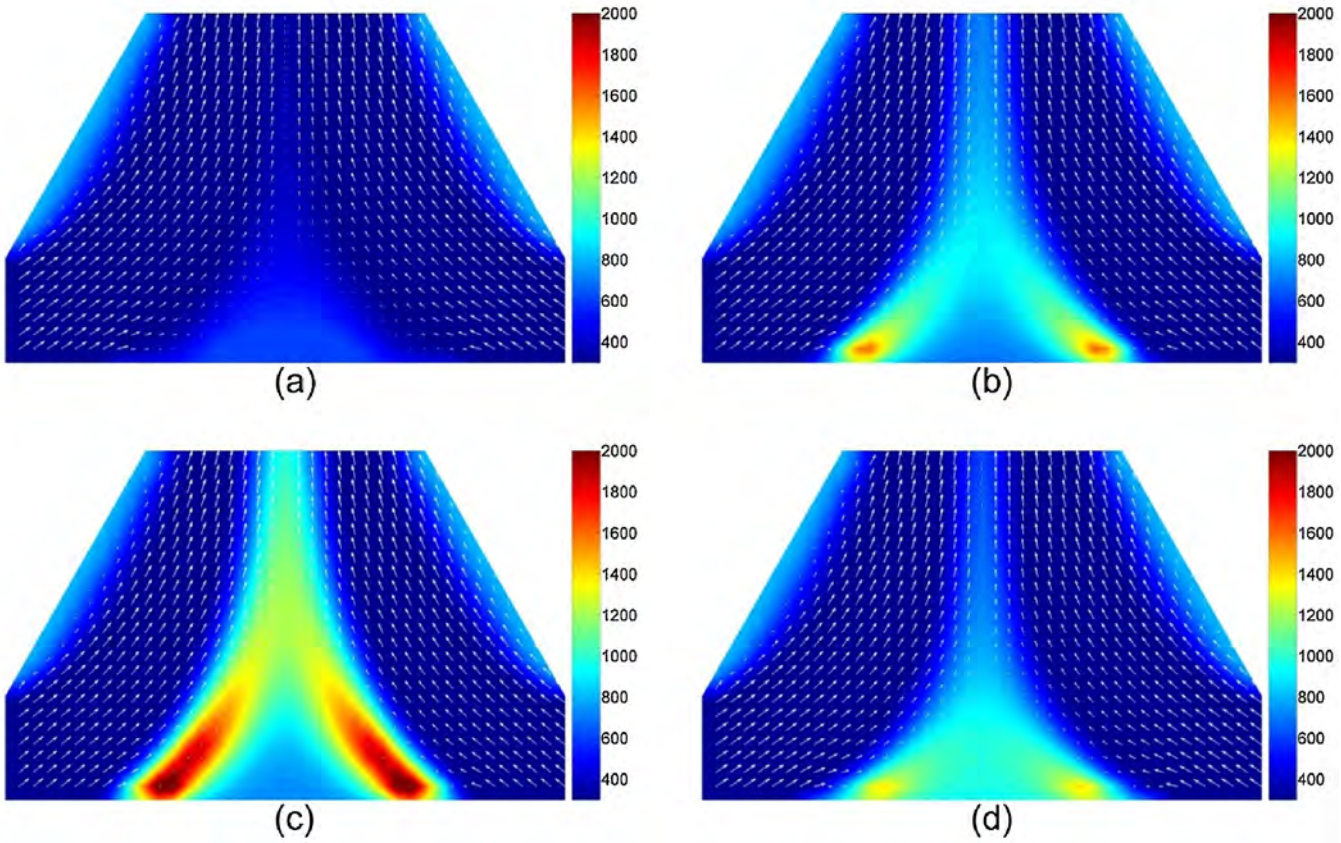

Fig. 5. Temperature and gas velocity in the gas phase for 10 mm thickness Cherry under 25 kW/m^2 heat flux at: (a) 200 s; (b) 400 s; (c) 500 s; and (d) 800 s.

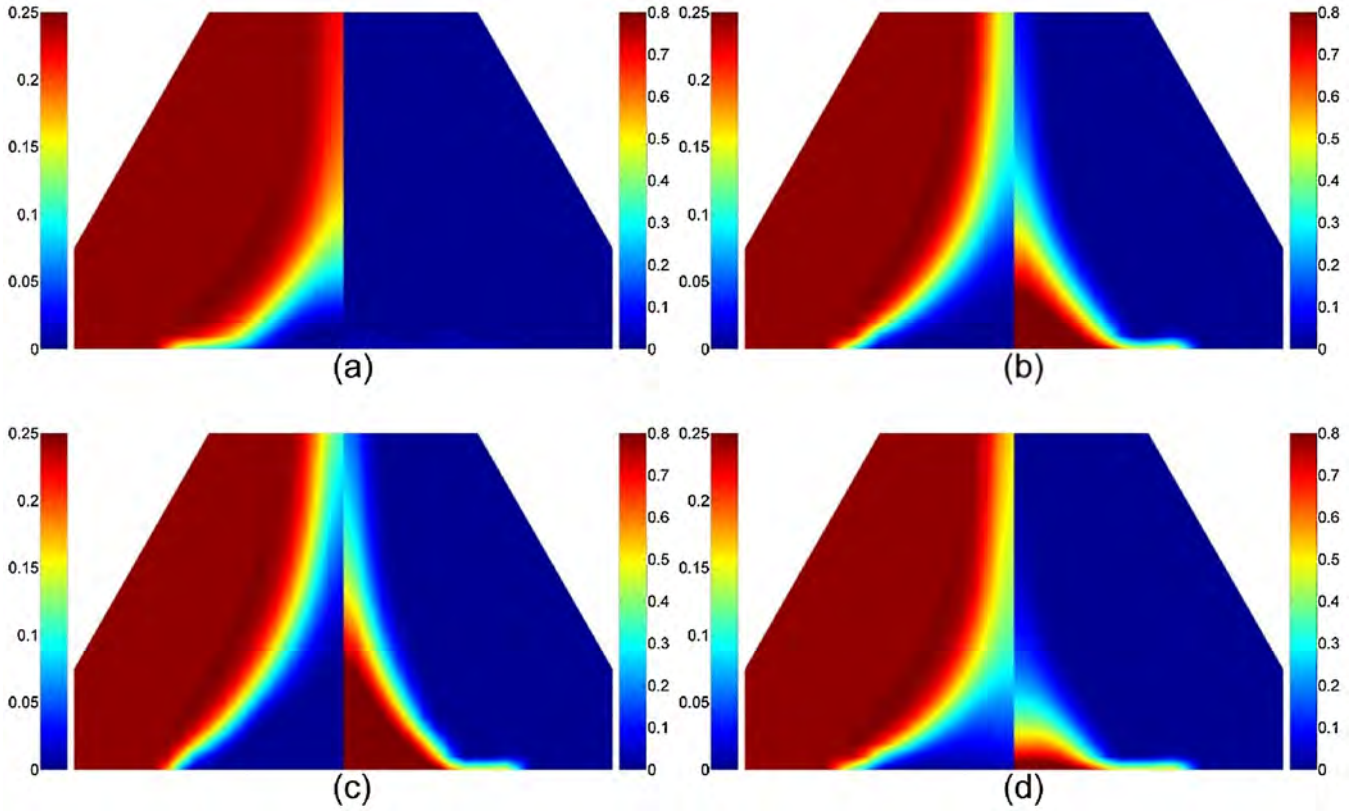

Fig. 6. Mass fraction of O_2 (left half) and Fuel (right half) in the gas phase for 10 mm thickness Cherry under 25 kW/m^2 heat flux at: (a) 200 s; (b) 400 s; (c) 500 s; and (d) 800 s.

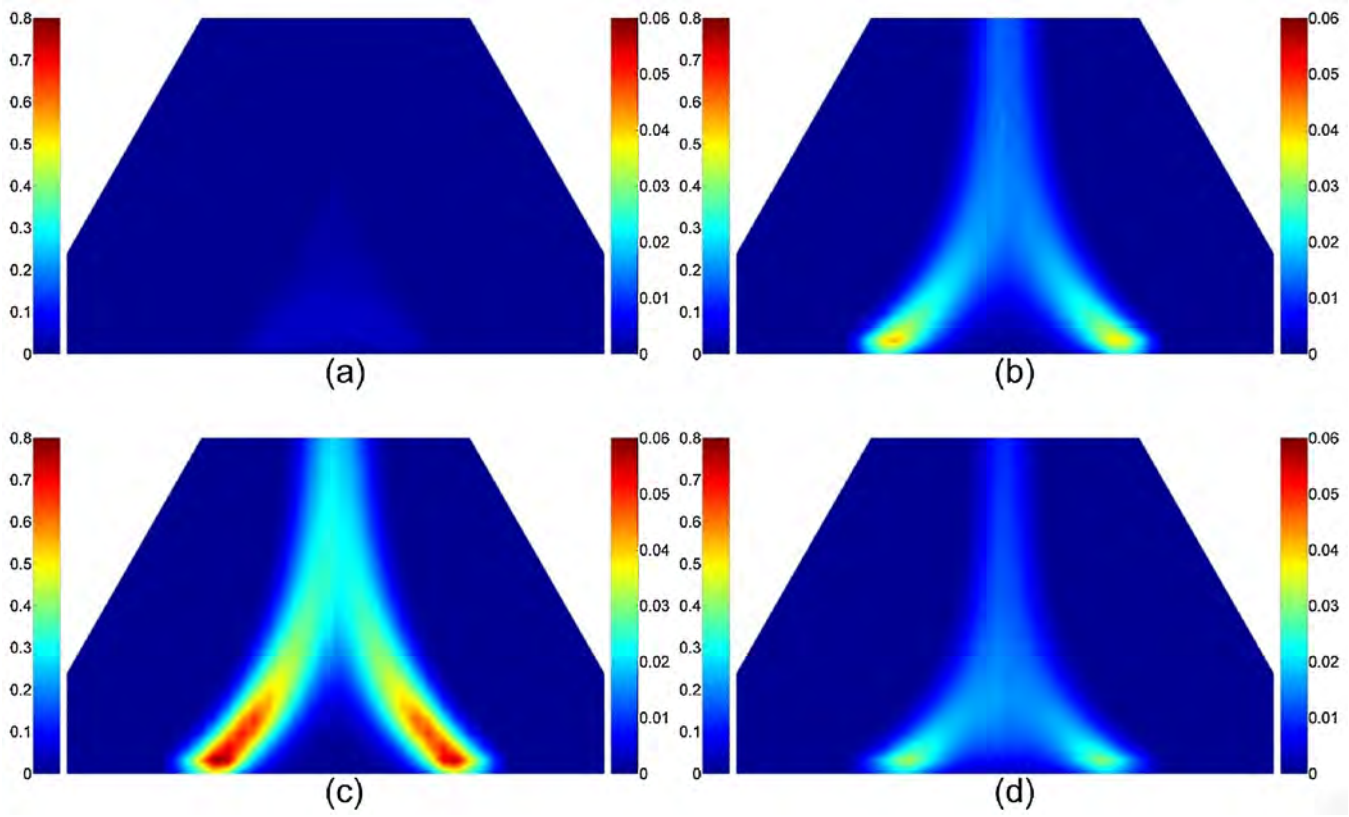

Fig. 7. Mass fraction of CO_2 (left half) and CO (right half) in the gas phase for 10 mm thickness Cherry under 25 kW/m^2 heat flux at: (a) 200 s; (b) 400 s; (c) 500 s; and (d) 800 s.

Table 2
Thermal properties of ABS for modeling input.

Property	Unit	ABS	Char/Ash
Pyrolysis reaction rate	1/s	9.50×10^{10} exp(-179.2×10^3/RT) [75]	1.31×10^8 exp(-134000/RT) [12]
Density	kg/m^3	1065.7 [Measured]	450 (Char); 155 (Ash)
Moisture content	kg/kg	–	–
Yield	kg/kg	0.20 (Char)	0.20 (Ash yield)
Heat of reaction	J/kg	6.0×10^5	9.8×10^5
Heat transfer coefficient	W/m^2 K	10	10
Gas permeability	m^2	5.80×10^{-17}	5.80×10^{-16}
Water permeability	m^2	3.79×10^{-20}	3.79×10^{-19}
Diffusion coefficient of water	m^2/s	5.11×10^{-9}	5.11×10^{-8}
Diffusion coefficient of gas	m^2/s	1.85×10^{-10}	1.85×10^{-9}
Specific heat capacity	J/kg K	1500 [76]	1350 [62]
Surface emissivity	–	0.95	0.8 [65]
Thermal conductivity	W/m K	0.45	0.35

3.3. Initial and boundary conditions

Initial gas pressure is equal to ambient $\rho|_{t=0} = \rho_0$ through the entire domain. Initial temperature is ambient temperature $T|_{t=0} = T_0$ everywhere.

Initial conditions of the solid phase are given

$$X|_{t=0} = X_0,\ \rho_s|_{t=0} = (1 - X_0)\,\rho_0,\ \rho_l|_{t=0} = X_0\rho_0,\ \rho_g|_{t=0} = \rho_{g,0},\ u_g|_{t=0} = u_l|_{t=0} = 0 \quad (24)$$

Initial conditions of the gas phase are provided

$$u|_{t=0} = 0,\ v|_{t=0} = 0,\ \rho|_{t=0} = \rho_0,\ Y_i|_{t=0} = Y_{i0} \quad (25)$$

Boundary conditions for the solid phase are given by

$$\lambda \frac{\partial T}{\partial x}\Big|_{x=L} = \dot{q}''_{ext} - h(T_{sur} - T_0) - \varepsilon\sigma({T_{sur}}^4 - {T_0}^4),\ \ \lambda \frac{\partial T}{\partial x}\Big|_{x=0} = 0 \quad (26)$$

$$P|_{x=L} = P_0,\ \frac{\partial P}{\partial x}\Big|_{x=0} = 0,\ \frac{\partial Y_i}{\partial x}\Big|_{x=L} = 0,\ \frac{\partial Y_i}{\partial x}\Big|_{x=0} = 0 \quad (27)$$

In the gas phase, the top open boundary conditions were set in terms of exit velocity v_{ex} of the gas leaving the heater. This velocity is determined by the volumetric extraction rate (24 L/s) through the hood that encloses the cone heater

$$u = 0,\ v = v_{ex},\ P = P_0 \quad (28)$$

Bottom and side open boundaries have the following conditions imposed on them

$$\frac{\partial u}{\partial x} = 0,\ \frac{\partial v}{\partial x} = 0,\ P = P_0 \quad (29)$$

Further, no-slip conditions are imposed on the solid boundaries (walls)

$$u = 0,\ v = 0,\ \frac{\partial P}{\partial x} = 0 \quad (30)$$

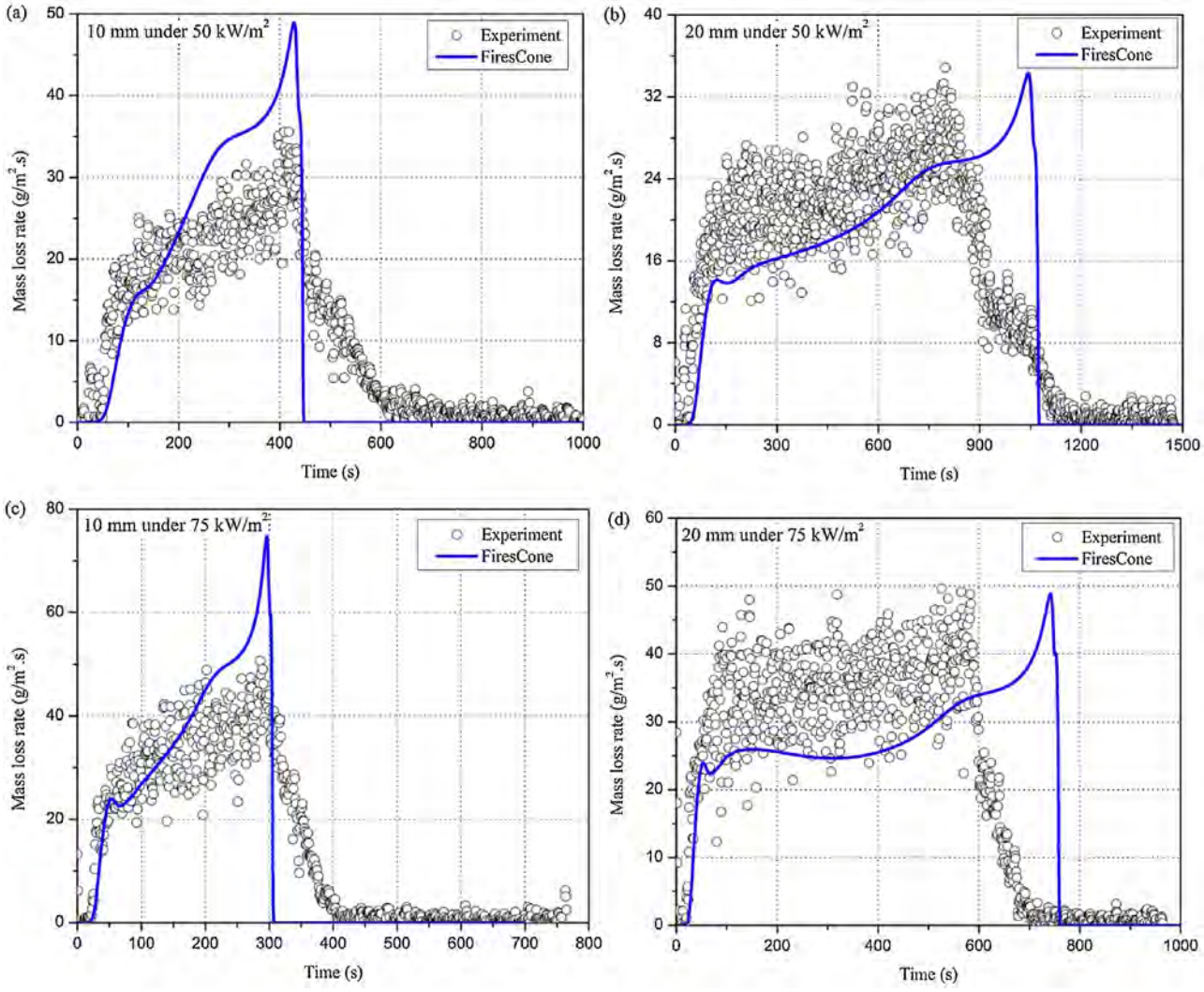

Fig. 8. Comparisons between modeling and experiments for 10 and 20 mm thick ABS under 50 and 75 kW/m^2 heat flux.

while mass flux of volatiles (obtained from solid phase calculations) $\dot{m}''_B$ serves as a velocity condition at the surface of the material

$$\dot{m}'' = \dot{m}''_B, \frac{\partial P}{\partial y} = 0 \tag{31}$$

Boundary conditions for the scalar quantities are

$$\frac{\partial T}{\partial x} = 0, \frac{\partial Y_i}{\partial x} = 0 \tag{32}$$

at the top open boundary

$$T = T_0, Y_i = Y_{i0} \tag{33}$$

at the bottom and side open boundaries, and finally

$$T = T_{sur}, \frac{\partial Y_i}{\partial x} = 0 \tag{34}$$

3.4. Numerical approach

Governing equations in both solid and gas phases were solved by fully implicit Finite Volume Method. Staggered grids were utilized to avoid oscillations and convergence problems for the pressure field [50]. Quadratic Upstream Interpolation for Convective Kinematics (QUICK) as a high order differencing scheme was utilized to discretize all convective terms as it includes the information of three control volumes from upstream [51]. Pressure Implicit with Splitting of Operators (PISO) was used to solve the pressure-velocity coupling problem [52].

The developed numerical model includes two parts, namely the sub-programs for solid and gas phases, respectively. The sub-program of solid phase was used to simulate pyrolysis processes of solid fuels under external radiations. Pyrolysis reactions of these solid fuels and their products, transportation processes of liquids and gases, and volume change were considered. The sub-program of gas phase was used to simulate combustion processes of those gas volatiles exhausted from the solid phase. These gas volatiles were produced from the pyrolysis reactions in the solid phase, which were then exhausted from the solid phase under the pressure and concentration gradients.

In the solid phase, it was indicated from sensitivity analysis that the surface temperature and mass loss rate were less influenced by the grid spacing less than 0.1 mm. Grid spacing of 2 and 4 mm were utilized for the sensitivity analysis of the gas phase modeling. Calculation time increases significantly when grid spacing decrease from 4 to 2 mm. It was noticed from the comparison of results over the first 50 s of calculations that these two grid spacing show little difference. Therefore, grid size of 4 mm was then used in the gas phase modeling.

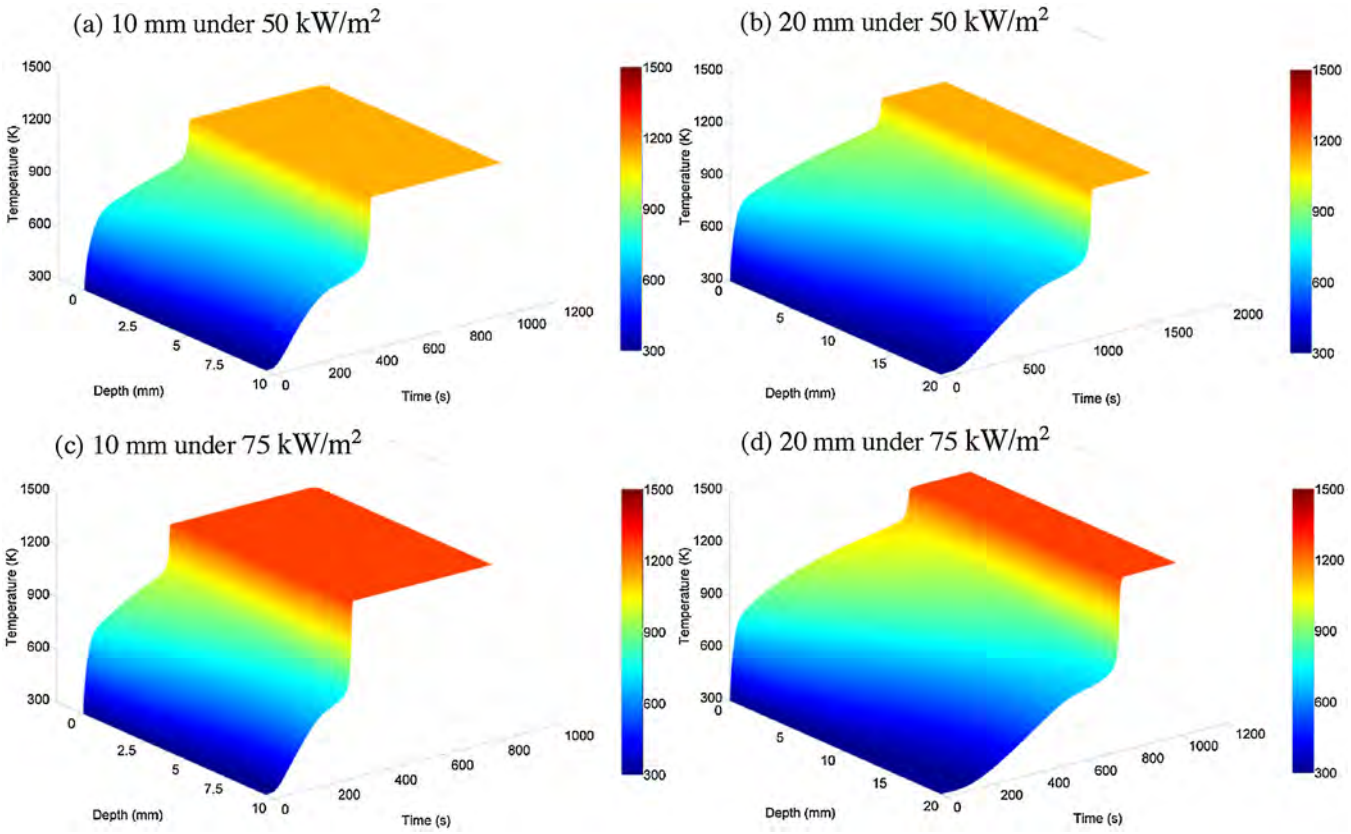

Fig. 9. Temperatures inside 10 and 20 mm thick ABS slabs under 50 and 75 kW/m^2 heat flux.

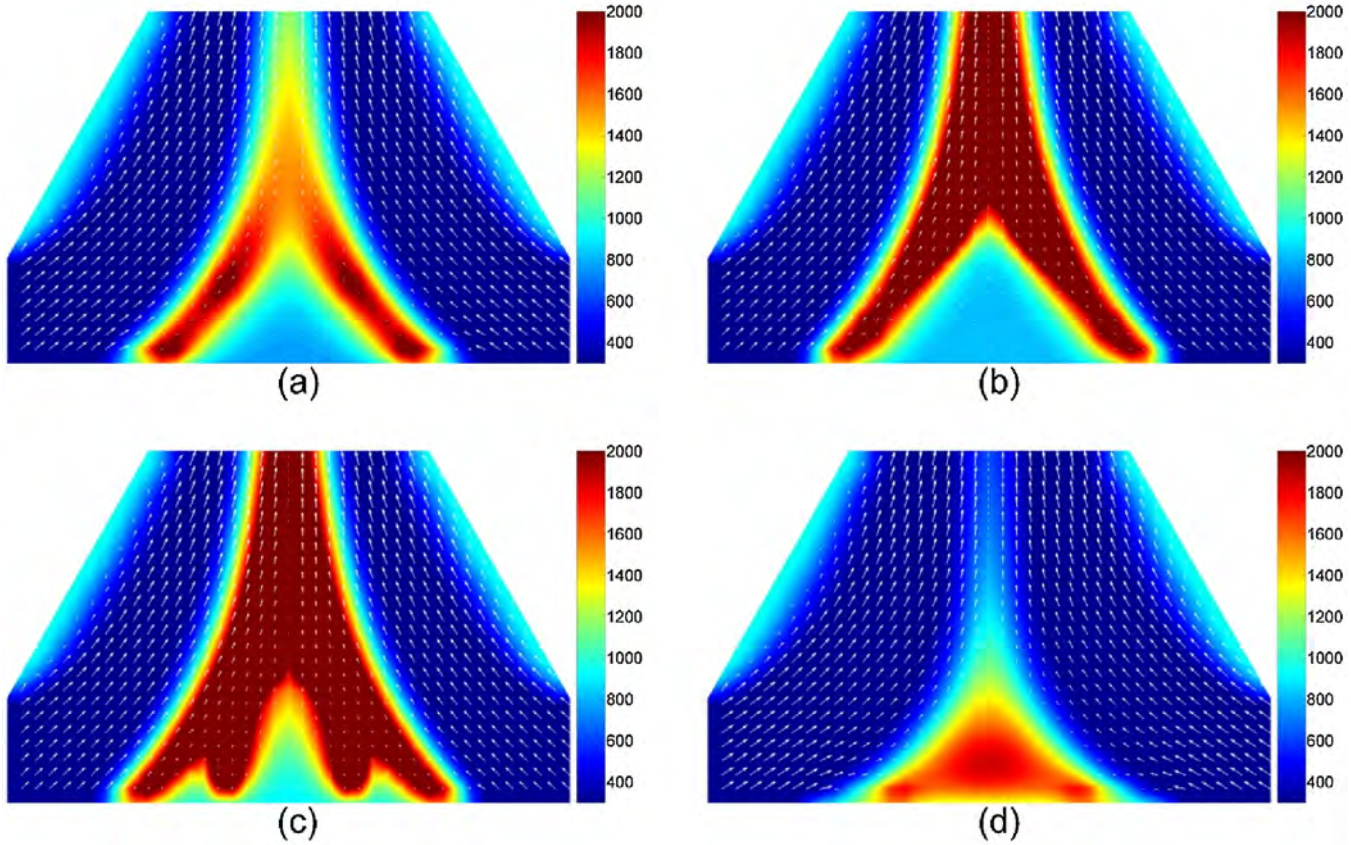

Fig. 10. Temperature and gas velocity in the gas phase for 10 mm thickness ABS under 50 kW/m^2 heat flux at: (a) 100 s; (b) 200 s; (c) 400 s; and (d) 600 s.

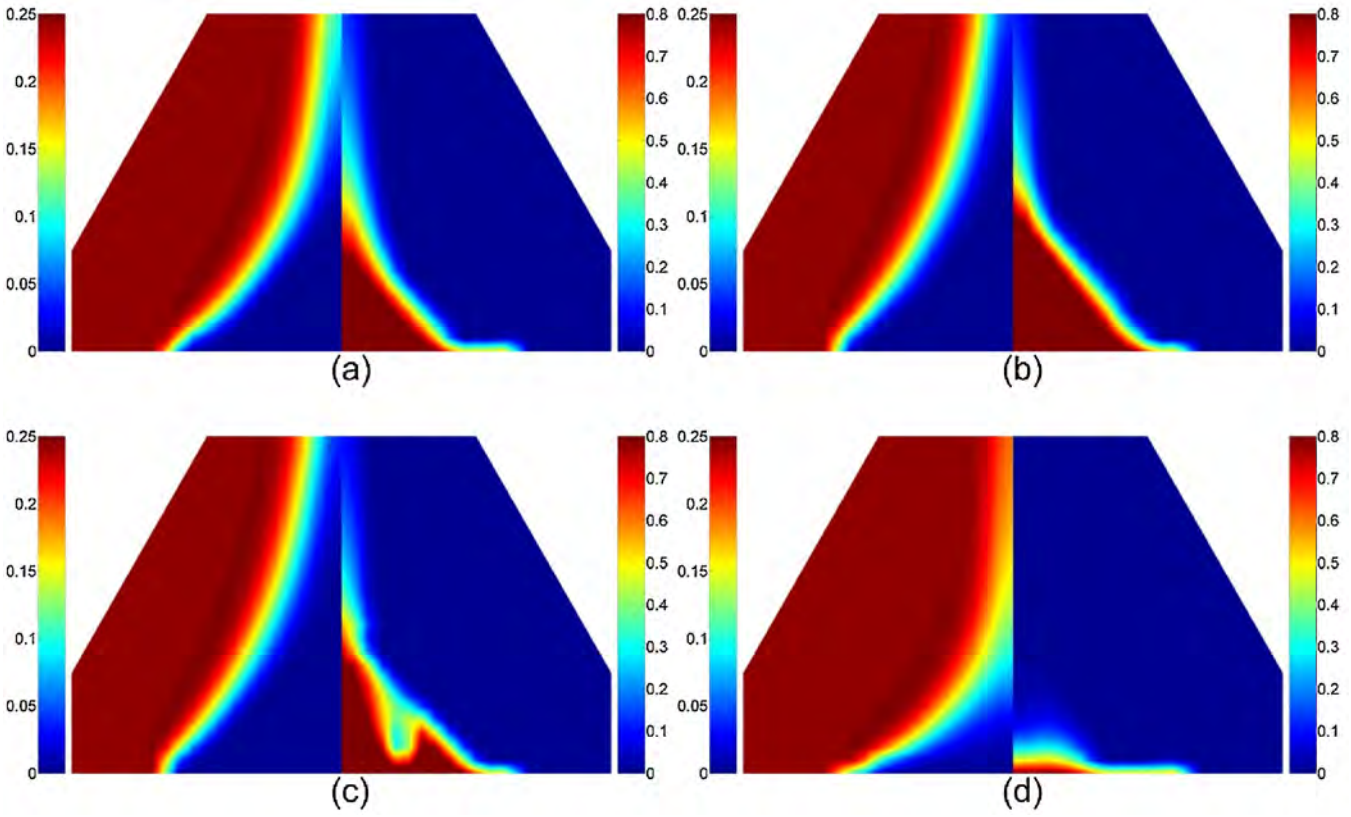

Fig. 11. Mass fraction of O_2 (left half) and Fuel (right half) in the gas phase for 10 mm thickness ABS under 50 kW/m^2 heat flux at: (a) 100 s; (b) 200 s; (c) 400 s; and (d) 600 s.

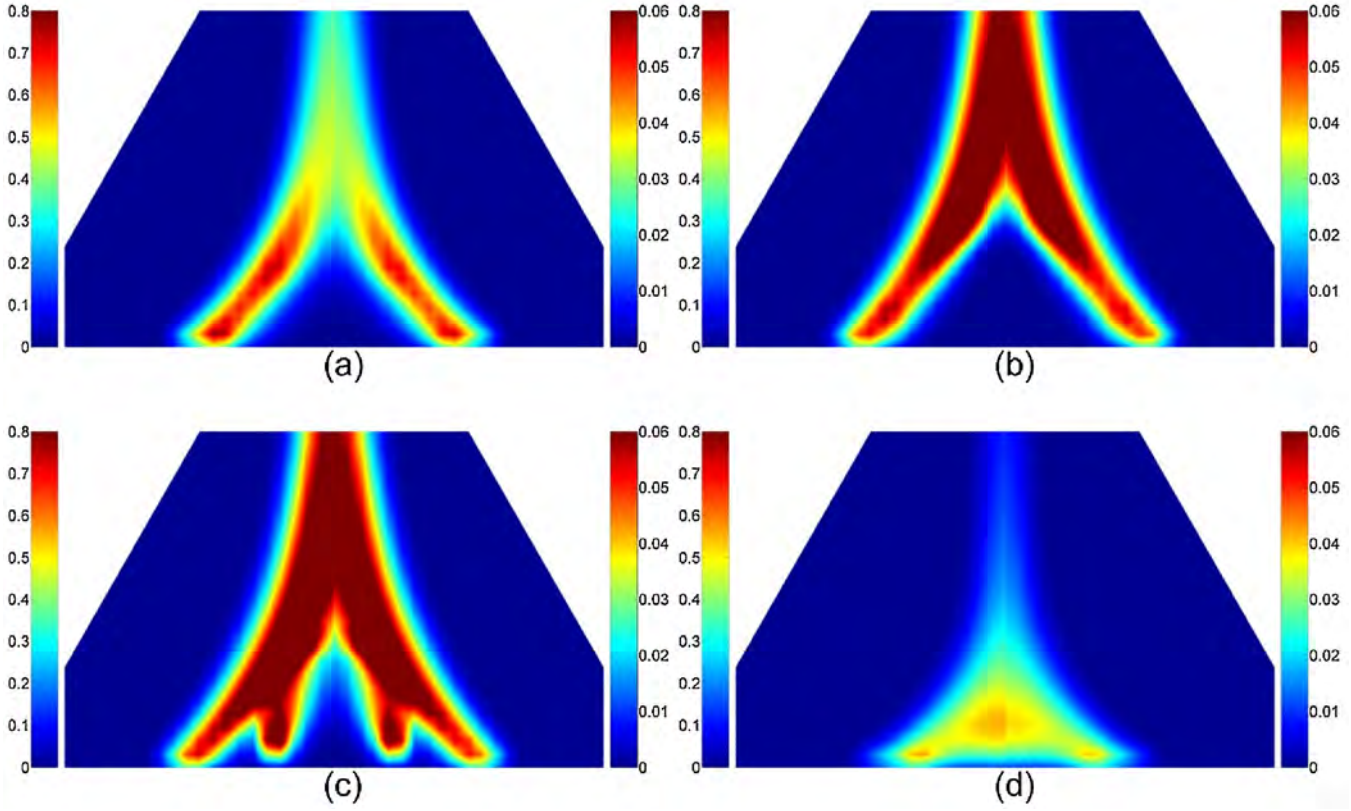

Fig. 12. Mass fraction of CO_2 (left half) and CO (right half) in gas phase for 10 mm thickness ABS under 50 kW/m^2 heat flux at: (a) 100 s; (b) 200 s; (c) 400 s; and (d) 600 s.

4. Results and discussion

All the data in this section were presented for three different levels of external radiation: low (25 kW/m^2), medium (50 kW/m^2) and high (75 kW/m^2). Two different values of the sample thickness are considered: 10 and 20 mm.

4.1. Timber

4.1.1. Thermal properties of Cherry

Cherry has been tested in a cone calorimeter to validate numerical modeling. Thermal properties of Cherry for modeling input are presented in Table 1. Five species are considered, namely virgin Cherry, char, ash, liquid water and gas volatiles (Fuel). Reactions of the form in Eq. (5) are considered

$$Cherry \rightarrow Char + Fuel \quad (35)$$

$$Char \rightarrow Ash + Fuel \quad (36)$$

4.1.2. Mass loss rate and solid phase temperature distribution

Mass loss rate (*MLR*) histories are primary data for comparison between numerical predictions and experiments, shown in Fig. 3. The labels in the subfigures show the thickness of the samples and external heat flux for experiments, same as follows. At all flux levels three different peaks of *MLR* are observed. The first peak occurs at a maximum rate of water evaporation, and just before the major timber pyrolysis reactions accelerate. Evaporation of water is significant when the slab temperature is above 100 °C [71]. The first peak degenerates into small plateau for the cases where both heat flux and sample thickness are either low (Fig. 3(a)) or high (Fig. 3(f)), but is clearly seen in other cases.

The second stage (between the first and the second peaks) reflects preliminary pyrolysis reactions of virgin Cherry. This stage generally starts once the temperature of the Cherry exceeds about 240 °C [72]. The third stage develops once heat wave inside the material penetrates towards its back surface. Insufficient heat loss through the back surface results in the development of the third peak. Pyrolysis of char also occurs at this stage. Global maximum of *MLR* is observed during this stage. The abrupt fall of computational *MLR* is due to the completion of all the pyrolysis reactions of virgin timber and char, with a small amount of ash left in the solid phase.

It was noted that mass loss due to water evaporation is much more obvious in the modeling, compared to the experiment (Fig. 3). This can be attributed to rather short period of water evaporation as moisture content represents small proportion of the sample's mass. Mass loss is hard to be measured in the experiment over short periods of time. Another reason is a possibility that some jump points in *MLR* history are effectively ignored upon smoothing by Savitzky-Golay method [73,74]. It should also be noticed that the time scale for these samples slabs are different, which is because the chemical reactions of the samples under different thicknesses and external radiation levels.

All the three levels of heat fluxes produce similar *MLR* data with magnitudes of the peaks increasing with higher intensity of external heating. Qualitatively, there is a good agreement between predictions and experimental data. Quantitative agreement is reasonable in most cases, but some deviations are observed in the magnitudes of the *MLR* peaks, as well as in times of *MLR* drop-offs after the maximum value. The discrepancies in the peak magnitudes are expected as chemical kinetics involved is quite complex and not understood completely. Drop-off times are essentially controlled by the heat transfer coefficient at the back surface of the material. This property needs be more accurately measured in order to achieve better agreement with experiments.

Temperatures distributions inside Cherry slabs under 25, 50 and 75 kW/m^2 heat fluxes are shown in Fig. 4. The axis X, Y and Z show the time, depth and temperature, respectively. The right color bar of each subfigure show a temperature range of 300–1500 K. General trends are quite obvious and consistent with expected observations of heat propagation into the solid substance. The process is affected under variable thermal conductivity and volume shrinkage. This means that heat gain rate per unit mass of material increases as the process progresses. Consequently, internal material temperature rise faster than it would if the material was chemically inert.

Due to adiabatic conditions (Eq. (26)) set at the back surface of the material, temperature inside the sample levels off at the end of the process, and the material eventually starts to behave as thermally thin. All the pyrolysis reactions finally stop due to consumption of virgin Cherry. Remaining ash approaches equilibrium conditions, as thermal radiation absorption and losses from the surface balance out.

Maximum temperatures for the two different sample thicknesses are very similar, but the time to achieve this maximum is obviously longer for the thicker sample. For example, for the 10 mm Cherry slab, surface temperature reaches maximum in about 300 s (Fig. 4(e)) under 75 kW/m^2 irradiance, and this time increases to about 800 s (Fig. 4), under 25 kW/m^2 heat flux. Observed differences between front and back surface temperatures are more significant at higher levels of external fluxes.

4.1.3. Diffusion flame predictions

Temperature and gas velocity fields in the gas phase under 25 kW/m^2 heat fluxes are presented in Fig. 5. Three high temperature areas are observed. The first two symmetrical areas are near the heaters. Air temperature near the heaters increases due to thermal conduction and convection. The third area represents diffusion flame which develops above the sample surface due to pyrolised material influx. Flame intensity increases with the intensity of external heat flux due to obvious increase in the pyrolysis rates. Flame becomes most detached from the surface at higher levels of pyrolysis rates (in conformity with *MLR* data, shown in Fig. 3), and attaches to the surface at later stages as pyrolysis reactions (and pyrolysis flux) cease.

Distributions of mass fractions of oxygen and fuel under 25 kW/m^2 heat flux are demonstrated in Fig. 6. Mass fractions of O_2 are close to ambient levels in most areas except the region above sample surface. This is consistent with the structure of diffusion flame and computational domain where fresh air can enter from both bottom corners. High fuel (pyrolysis products) concentrations are located above the surface of the material. Fuel mass fraction profiles are shaped by the two competitive processes, that is the rate of volatiles release form the solid phase, and the rate of fuel consumption in the flame.

Distribution of combustion products (CO and CO_2) can be seen in Fig. 7. Overall, both species concentrations show qualitatively similar profiles over the considered range of external heat fluxes. This is a result of the prescribed split between combustion products in the global chemical reaction shown in Eq. (5). Mass fractions contours of CO and CO_2 also show similarity with the temperature contours in Fig. 5. This is expected correlation as both energy release rates and species production are related to the rates of combustion, giving rise to quasi-similarity between temperature and concentration fields in diffusion flames.

4.2. Charring polymer

4.2.1. Thermal properties of ABS

In the second set of experiments a charring polymer ABS has been tested in cone calorimeter for the validation of the developed

model. Pyrolysis reactions of ABS, which are accounted by Eq. (1), in this case, represent the following transformations:

$$ABS \rightarrow Char + Fuel \quad (37)$$

$$Char \rightarrow Ash + Fuel \quad (38)$$

Reaction shown in Eq. (5) applies in the gaseous phase. As the moisture in the ABS can be ignored, the related evaporation process was not considered during the numerical modeling.

Table 2 shows thermal properties of ABS for modeling input. It should be noted that although in general the char residue from ABS is not the same as the char, no data has been found for the properties of char and ash produced by ABS. Therefore, such properties were taken as those of the timber. Same remark applies to the properties describing transport processes of liquids and gases through ABS media, such as diffusion coefficients and permeability. Such properties were also assumed based on the data for Cherry.

4.2.2. Mass loss rate and solid phase temperature distributions

In contrast to timber, ABS appeared to be highly dependent on the level of heat flux applied. Specifically, the 10 mm sample was not ignited under the lower 25 kW/m^2 heat flux, while modeling showed ignition and significant peak *MLR*. This case could not be modeled properly as the chosen flux value appears to be very close for the critical heat flux for ABS. For the 20 mm sample ignition occurred after a very substantial delay, and the process could not be modeled accurately either. Therefore, at the specified conditions, the combustion system is intrinsically unstable and the current mathematical model is not expected to perform well. So the following analysis will much focus on the fire behaviors under high heat fluxes.

Fig. 8 shows the comparisons between modeling and experiments for ABS under 50 kW/m^2 and 75 kW/m^2 heat fluxes. As evident from these figures, thermal degradation of ABS follows three major stages. First is the rapid ignition, accompanied by significant increase in *MLR*. The second stage, involving both pyrolysis reactions of virgin ABS and char oxidation, shows much smoother *MLR* profile. Peak of *MLR* is achieved at the end of this stage (due to adiabatic conditions at the back of the sample's surface), and the third stage demonstrates fall in the *MLR* until the point of full conversion of virgin ABS into char, and subsequent total combustibles consumption. The first two stages are reproduced by the model reasonably well, although peak *MLR* is generally overestimated. The third stage is not reproduced well as the modeled *MLR* drops abruptly to zero level, rather than following less steeply declining experimental profiles. Apart from potentially not fully accurate boundary condition at the back surface, it is believed that the lack of accurate kinetic data on char oxidation contributes to this discrepancy as well. Once such data becomes available, the modeling results are likely to be improved.

ABS slabs temperature distribution, in the direction transversal to the surface under 50 and 75 kW/m^2 heat fluxes are shown in Fig. 9. Similar to Cherry, surface temperature increases rapidly as the heating starts. Rate of temperature rise at the back surface is much slower due to substantial heat penetration time, which becomes longer for a thicker sample. Maximum temperatures occur once all the virgin ABS turns into ash. These peak temperatures increase with the raising levels of external heat flux.

4.2.3. Diffusion flame predictions

Fig. 10 shows flow temperature and velocities under 50 kW/m^2 heat fluxes, respectively. Similar to Cherry tests, high temperature areas are located near the heater and close to sample surface. Behavior of flames is very similar to the case of the timber sample. Flame essentially becomes detached from the surface upon ignition, while the hottest region of the flame descends towards the material surface before the extinction. Mass fractions of oxygen and fuel shown in Fig. 11, as well as those of products (CO and CO_2 shown in Fig. 12) essentially follow the same trend, as in the case of Cherry combustion.

Mass loss rate (in the above specified range of external radiative fluxes) is effectively dictated by the level of external radiation and properties of the solid fuel. Consequently, effects of combustion, turbulence and radiation transfer in the gas phase are also of secondary importance in basic material tests under cone calorimeter [77]. The implication of this finding is that sophisticated computational models developed for treatment of thermal degradation of various materials may be validated against experiments without spending much effort and time on predicting diffusion flame behavior. In real fire prediction, of course, fully coupled treatment of both the phases is necessary.

5. Conclusions

Frequently used building materials such as charring materials were investigated on their fire behaviours under external radiance both experimentally and numerically. Two typical charring materials were selected in this study, including timber (Cherry) and acrylonitrile butadiene styrene (ABS). The proposed numerical model has considered both solid and gas phases, which were validated by cone calorimeter experiments. Predictions of mass loss rate agree reasonably well with experimental data in nearly all the cases, except for the ABS under low radiative heat flux. In general, three different stages of mass loss rate histories are observed, in agreement with the previous studies. Global peak of the mass loss rate occurs near the end of the process, followed by rapid descend of mass loss rate. Diffusion flame has been reproduced in calculations, as well as details of flame chemistry and flow turbulence. Major modelling emphasis in reproducing cone calorimeter test should be made on modeling physical and chemical processes occurring in the solid phase. It provides an excellent basis to investigate the fire behavior of building materials.

This study provides an attempt for the combination of both solid and gas phase modeling. One limitation of this study is the validation of gas phase modeling, which will be taken when the related experimental conditions are allowed. Another limitation is the absent consideration of flame radiation, which will be carried out in our future research after validating the gas phase modeling of building materials.

References

[1] M. Asif, T. Muneer, R. Kelley, Life cycle assessment: a case study of a dwelling home in Scotland, Build. Environ. 42 (3) (2007) 1391–1394.
[2] H. Islam, M. Jollands, S. Setunge, N. Haque, M.A. Bhuiyan, Life cycle assessment and life cycle cost implications for roofing and floor designs in residential buildings, Energy Build. 104 (2015) 250–263.
[3] M.M. Hassan, Mechanical, thermal, and morphological behavior of the polyamide 6/acrylonitrile–butadiene–styrene blends irradiated with gamma rays, Polym. Eng. Sci. 48 (2) (2008) 373–380.
[4] N. Werther, S. Winter, Proceedings of the 1st European Workshop Fire Safety of Green Buildings, in: The 1st European Workshop Fire Safety of Green Buildings, Berlin, Germany, 2015.
[5] S.L. Xu, L.X. Zhang, Y.J. Lin, R.S. Li, F.Z. Zhang, Layered double hydroxides used as flame retardant for engineering plastic acrylonitrile–butadiene–styrene (ABS), J. Phys. Chem. Solids 73 (12) (2012) 1514–1517.
[6] H. Biteau, A. Fuentes, G. Marlair, S. Brohez, J.L. Torero, Ability of the Fire Propagation Apparatus to characterise the heat release rate of energetic materials, J. Hazard. Mater. 166 (2–3) (2009) 916–924.
[7] D.K. Shen, S. Gu, K.H. Luo, A.V. Bridgwater, Analysis of wood structural changes under thermal radiation, Energy Fuels 23 (2) (2009).
[8] Y.B. Yang, A.N. Phan, C. Ryu, V. Sharifi, J. Swithenbank, Mathematical modelling of slow pyrolysis of segregated solid wastes in a packed-bed pyrolyser, Fuel 86 (2007) 169–180.
[9] L. Shi, M.Y.L. Chew, A review of fire processes modeling of combustible materials under external heat flux, Fuel 106 (2013) 30–50.

[10] J.H. Wang, G.Q. Li, L. Shi, Y. Jiao, Q.M. Xie, Transport time lag effect on smoke flow characteristics in long-narrow spaces, Fire Technol. (2016), http://dx.doi.org/10.1007/s10694-016-0614-2.
[11] R. Tarchini, A. Galgano, C. Di Blasi, Modeling the influences of pressure and velocity variations on the microwave-induced pyrolysis of wood, AIChE J. 58 (2012) 610–624.
[12] C. Di Blasi, Combustion and gasification rates of lignocellulosic chars, Prog. Energy Combust. Sci. 35 (2) (2009) 121–140.
[13] F. Jia, E.R. Galea, M.K. Patel, The numerical simulation of the noncharring pyrolysis process and fire development within a compartment, Appl. Math. Modell. 23 (1999) 587–607.
[14] K.D. Steckler, T. Kashiwagi, H.R. Baum, Analytical model for transient gasification of noncharring thermoplastic materials, in: The Third International Symposium of Fire Safety Science, University of Edinburgh, 1991, pp. 895–904.
[15] C. Di Blasi, A. Galgano, C. Branca, Modeling the thermal degradation of poly(methyl methacrylate)/carbon nanotube nanocomposites, Polym. Degrad. Stab. 98 (2013) 266–275.
[16] A. Galgano, C. Di Blasi, E. Milella, Sensitivity analysis of a predictive model for the fire behaviour of a sandwich panel, Polym. Degrad. Stab. 95 (2010) 2430–2444.
[17] Y. Zhang, Y.C. Wang, C.G. Bailey, A.P. Taylor, Global modelling of fire protection performance of an intumescent coating under different furnace fire conditions, J. Fire Sci. 50 (2012) 51–62.
[18] C. Lautenberger, C. Fernandez-Pello, Generalized pyrolysis model for combustible solids, Fire Saf. J. 44 (2009) 819–839.
[19] S.I. Stoliarov, S. Crowley, R.N. Walters, R.E. Lyon, Prediction of the burning rates of charring polymers, Combust. Flame 157 (11) (2010) 2024–2034.
[20] M.A. Hastaoglu, F. Berruti, A gas-solid reaction model for flash wood pyrolysis, Fuel 68 (1989) 1408–1415.
[21] J. Larfeldt, B. Leckner, M.C. Melaaen, Modelling and measurements of drying and pyrolysis of large wood particles, in: Progress in Thermochemical Biomass Conversion, 2008, pp. 1046–1060.
[22] M. Bellais, Modelling of the Pyrolysis of Large Wood Particles, Department of Chemical Engineering and Technology, Royal Institute of Technology, 2007.
[23] M. Bellais, K.O. Davidsson, T. Liliedahl, K. Sjostrom, J.B.C. Pettersson, Pyrolysis of large wood particles: a study of shrinkage importance in simulations, Fuel 82 (2003) 1541–1548.
[24] C. Di Blasi, Modeling the effects of high radiative heat fluxes on intumescent material decomposition, J. Anal. Appl. Pyrol. 71 (2004) 721–737.
[25] R.M. Sullivan, N.J. Salamon, A finite element method for the thermochemical decomposition of polymeric materials – I. Theory, Int. J. Eng. Sci. 30 (1992) 431–441.
[26] J. Lede, Reaction temperature of solid particles undergoing an endothermal volatilization: application to the fast pyrolysis of biomass, Biomass Bioenergy 7 (1994) 49–60.
[27] P. Gu, R.J. Asaro, Designing sandwich polymer matrix composite panels for structural integrity in fire, Compos. Struct. 88 (2009) 461–467.
[28] K.M. Bryden, M. Hagge, Modeling the combined impact of moisture and char shrinkage on the pyrolysis of biomass particle, Fuel 82 (2003) 1633–1644.
[29] S. Feih, Z. Mathys, A.G. Gibson, A.P. Mouritz, Modelling the compression strength of polymer laminates in fire, Compos. Part A 38 (2007) 2354–2365.
[30] C.S. Luo, J. Lue, P.E. DesJardin, Thermo-mechanical damage modeling of polymer matrix sandwich composites in fire, Compos. Part A 43 (5) (2012) 814–821.
[31] J.E.J. Staggs, A simple model of polymer pyrolysis including transport of volatiles, Fire Saf. J. 34 (2000) 69–80.
[32] K.M. Bryden, K.W. Ragland, C. Rutland, Modeling thermally thick pyrolysis of wood, Biomass Bioenergy 22 (2002) 41–53.
[33] D.K. Shen, M.X. Fang, Z.Y. Luo, K.F. Cen, Modeling pyrolysis of wet wood under external heat flux, Fire Saf. J. 42 (2007) 210–217.
[34] J.B. Henderson, T.E. Wiecek, A mathematical model to predict the thermal response of decomposing, expanding polymer composites, J. Compos. Mater. 21 (1987) 373–393.
[35] R. Hilbert, F. Tap, H. El-Rabii, D. Thevenin, Impact of detailed chemistry and transport models on turbulent combustion simulations, Prog. Energy Combust. Sci. 30 (2004) 61–117.
[36] R. Vijeu, L. Gerun, M. Tazerout, C. Castelain, J. Bellettre, Dimensional modelling of wood pyrolysis using a nodal approach, Fuel 87 (2008) 3292–3303.
[37] Y.F. Wang, L.Z. Yang, X.D. Zhou, J.K. Dai, Y.P. Zhou, Z.H. Deng, Experiment study of the altitude effects on spontaneous ignition characteristics of wood, Fuel 89 (2010) 1029–1034.
[38] G.T. Linteris, L. Gewuerz, K. McGrattan, G. Forney, Modeling Solid Sample Burning with FDS, National Institute of Standards and Technology, 2004.
[39] ISO 5660-1, Reaction to fire tests – heat release, smoke production and mass loss rate – Part 1 Heat release rate (cone calorimeter method), in, 2002.
[40] L. Shi, M.Y.L. Chew, Fire behaviors of polymers under autoignition conditions in a cone calorimeter, Fire Saf. J. 61 (2013) 243–253.
[41] L. Shi, M.Y.L. Chew, Experimental study of carbon monoxide for woods under spontaneous ignition condition, Fuel 102 (2012) 709–715.
[42] L. Shi, M.Y.L. Chew, V. Novozhilov, P. Joseph, Modelling the pyrolysis and combustion behaviours of non-charring and intumescent-protected polymers using 'FiresCone', Polymers 7 (2015) 1979–1997.
[43] L. Shi, M.Y.L. Chew, V. Novozhilov, A model to predict fire behaviors of combustible materials under external heat flux, in: The 14th International Conference and Exhibition on Fire and Materials, San Francisco, USA, 2015, pp. 256–270.
[44] F. He, F. Behrendt, A new method for simulating the combustion of a large biomass particle – a combination of a volume reaction model and front reaction approximation, Combust. Flame 158 (12) (2011) 2500–2511.
[45] C. Di Blasi, Modeling chemical and physical processes of wood and biomass pyrolysis, Prog. Energy Combust. Sci. 34 (2008) 47–90.
[46] J. Swann, J. Hartman, C. Beyler, Study of radiant smoldering ignition of plywood subjected to prolonged heating using the cone calorimeter, TGA, and DSC, in: The Ninth International Symposium on Fire Safety Science, German, 2008, pp. 98–102.
[47] P. Grammelis, P. Basinas, A. Malliopoulou, G. Sakellaropoulos, Pyrolysis kinetics and combustion characteristics of waste recovered fuels, Fuel 88 (1) (2009) 195–205.
[48] B.M. Suleiman, J. Larfeldt, B. Leckner, M. Gustavsson, Thermal conductivity and diffusivity of wood, Wood Sci. Technol. 33 (1999) 465–473.
[49] E. Ranzi, M. Corbetta, F. Manenti, S. Pierucci, Kinetic modeling of the thermal degradation and combustion of biomass, Chem. Eng. Sci. 110 (2014) 2–12.
[50] A. Kurganov, C.T. Lin, On the reduction of numerical dissipation in central-upwind schemes, Commun. Comput. Phys. 2 (1) (2007) 141–163.
[51] Z.P. Wei, Y.F. Jia, A depth-integrated non-hydrostatic finite element model for wave propagation, Int. J. Numer. Methods Fluids 73 (11) (2013) 976–10000.
[52] E.M.A. Frederix, M. Stanic, A.K. Kuczaj, M. Nordlund, B.J. Geurts, Extension of the compressible PISO algorithm to single-species aerosol formation and transport, Int. J. Multiphase Flow 74 (2015) 184–194.
[53] C. Lautenberger, C. Fernandez-Pello, A model for the oxidative pyrolysis of wood, Combust. Flame 156 (2009) 1503–1513.
[54] T. Hakkarainen, Post-flashover fires in light and heavy timber construction compartments, J. Fire Sci. 20 (2002) 133–175.
[55] W.C.R. Chan, M. Kelbon, B.B. Krieger, Modelling and experimental verification of physical and chemical processes during pyrolysis of a large biomass particle, Fuel 64 (1985) 1505–1513.
[56] R.S. Tang, Y. Etzion, Comparative studies on the water evaporation rate from a wetted surface and that from a free water surface, Build. Environ. 39 (2004) 77–86.
[57] J. Zhang, M.A. Delichatsios, Determination of the convective heat transfer coefficient in three-dimensiona inverse heat conduction problem, Fire Saf. J. 44 (2009) 681–690.
[58] S. Raji, Y. Jannot, P. Lagiere, J.R. Puiggali, Thermophysical characterization of a laminated solid-wood pine wall, Constr. Build. Mater. 23 (2009) 3189–3195.
[59] M. Anne Palin, J.A. Petty, Permeability to water of the wood cell wall and its variation with temperature, Wood Sci. Technol. 17 (1983) 187–193.
[60] H.I. Huang, K.V. Sarkanen, L.N. Johanson, Diffusion of dissolved oxygen in liquid-saturated Douglas fir sapwood, Wood Sci. Technol. 11 (3) (1977) 225–236.
[61] M.J. Spearpoint, J.G. Quintiere, Predicting the burning of wood using an integral model, Combust. Flame 123 (2000) 308–324.
[62] S.S. Alves, J.L. Figueiredo, A model for pyrolysis of wet wood, Chem. Eng. Sci. 44 (1989) 2861–2869.
[63] J. Suurkuusk, I. Wadso, Design and testing of an improved precise drop calorimeter for the measurement of the heat capacity of small samples, J. Chem. Thermodyn. 6 (1974) 667–679.
[64] D. Schmal, J.H. Duyzer, J.W. van Heuven, A model for the spontaneous heating of coal, Fuel 64 (1985) 963–972.
[65] K.W. Ragland, D.J. Aerts, Properties of wood for combustion analysis, Bioresour. Technol. 37 (1991) 161–168.
[66] K. Masuda, T. Takashima, Y. Takayama, Emissivity of pure and sea waters for the model sea surface in the infrared window regions, Remote Sens. Environ. 24 (1988) 313–329.
[67] M.G. Gronli, M.C. Melaaen, Mathematical model for wood pyrolysis – comparison of experimental measurements with model predictions, Energy Fuels 14 (2000) 791–800.
[68] M.L.V. Ramires, C.A. Nieto de Castro, Y. Nagasaka, A. Nagashima, M.J. Assael, W.A. Wakeham, Standard reference data for the thermal conductivity of water, J. Phys. Chem. Ref. Data 24 (1995) 1377–1381.
[69] J. Kestin, M. Sokolov, W.A. Wakeham, Viscosity of liquid water in the range −8 °C to 150 °C, J. Phys. Chem. Ref. Data 7 (1978) 941–948.
[70] P.K. Sinha, C.Y. Wang, Pore-network modeling of liquid water transport in gas diffusion layer of a polymer electrolyte fuel cell, Electrochim. Acta 52 (2007) 7936–7945.
[71] L. Shi, M.Y.L. Chew, Experimental study of woods under external heat flux by autoignition: ignition time and mass loss rate, J. Therm. Anal. Calorim. 111 (2) (2013) 1399–1407.
[72] M. Janssens, B. Douglas, Wood and wood products, in: Handbook of Building Materials for Fire Protection, McGraw-Hill, New York, 2004, pp. 7.1–7.58.
[73] J.W. Luo, K. Ying, J. Bai, Savitzky-Golay smoothing and differentiation filter for even number data, Signal Process. 85 (7) (2005) 1429–1434.
[74] L. Shi, M.Y.L. Chew, Influence of moisture on autoignition of woods in cone calorimeter, J. Fire Sci. 30 (2) (2012) 158–169.
[75] C.H. Wu, C.Y. Chang, J.L. Hor, S.M. Shih, L.W. Chen, F.W. Chang, On the thermal treatment of plastic mixtures of MSW: pyrolysis kinetics, Waste Manage. 13 (1993) 221–235.
[76] R.E. Lyon, M.L. Janssens, Polymer Flammability, Federal Aviation Administration, Washington D.C, 2005.
[77] V. Novozhilov, B. Moghtaderi, D.F. Fletcher, J.H. Kent, Computational fluid dynamics modelling of wood combustion, Fire Saf. J. 27 (1996) 69–84.